STUDIES ON NOVEL FRACTAL-TEXTURED SOLAR ABSORBER SURFACES FOR CONCENTRATED SOLAR POWER

K. Kant, K.P. Sibin, R. Pitchumani*

Advanced Materials and Technologies Laboratory

Department of Mechanical Engineering

Virginia Tech, Blacksburg, Virginia 24061-0238, United States

ABSTRACT

The solar absorptance of a thermal receiver surface significantly affects the photothermal conversion efficiency of concentrated solar power (CSP) plants. The development of low-cost Gen3 CSP systems calls for increasing the solar absorptance of the thermal receivers at operating temperatures above 750 °C. This study presents an innovative approach to the fractal, multiscale texturing of absorber surfaces to significantly enhance solar energy absorption for Gen3 CSP applications. The absorber surface is described in terms of its fractal parameters that are uniquely determined from surface profile measurements. The interaction of solar radiation with the fractal surface is numerically simulated by solving the governing Maxwell's equations for electromagnetic wave propagation to investigate the effect of texturing on the absorptance of the surfaces. It is shown that absorption of the solar spectrum increases with an increase in the fractal dimension and the multiscale asperity height of the surface texturing. The theoretical model is demonstrated to be in close agreement with experimental measurements of spectral absorptance of electrodeposited copper (Cu), copper mono-oxide (CuO), and copper-manganese oxide (CuMnO) surfaces that are textured to produce a range of fractal parameters by tailoring the deposition parameters. Fractal surface texturing is shown to reduce reflectance by over one order of magnitude, yielding an absorptance of greater than 0.985 for CuMnO. For the first time, the study presents a significant effective means of increasing solar absorptance and a fundamental theoretical description of the underlying physics.

Keywords: Fractal Texturing; Absorptance; Solar Selective Coatings; Concentrating Solar Power; Numerical Simulation

* Corresponding author; e-mail: pitchu@vt.edu

1. INTRODUCTION

The environmental crisis and increasing energy usage worldwide have led to the increasing adoption of renewable energy sources [1–3]. In their roadmaps, the European Union (EU) and the United States (US) each have plans to increase their renewable energy shares to 100% [4] and 80% [5], respectively, by 2050. Wind and solar energy are two valuable resources that will play a crucial role in achieving the objectives. In particular, many studies have reported the value of concentrating solar power (CSP) with thermal energy storage (TES) in meeting the renewable energy penetration goals [1,3,6–8]. The processes involved during the operation of the CSP plant are: concentration of sunlight onto solar receiver; absorption of incident solar radiation by the receiver and conversion of solar energy to heat; transfer of generated heat utilizing heat transfer fluid; power production by utilizing thermal energy in a heat engine and storage of excess heat in and efficient thermal energy storage [9].

The role of the thermal receiver in a CSP plant is to absorb sunlight efficiently with minimum thermal losses. To this end, enhancing the photothermal conversion efficiency of the receiver in the CSP systems is of significant interest [10–13], which mainly depends on the solar absorptance of the surface that communicates the energy of the incoming solar radiation to the heat transfer fluid (HTF). A high absorptance (>0.95) of the solar receiver is desired for visible and near-infrared (IR) wavelengths (0.28–2.5 μm), where the bulk of the energy from the solar spectrum is concentrated. Further, a low emittance is desired in the IR wavelengths (~ 2–20 μm), where the black body emission peaks [9]. Solar absorber materials are normally coated onto the base metal of the receivers to give the optimal optical properties. Several solar absorber coatings with different properties and materials have recently been produced using various fabrication techniques [9–13].

Solar absorptance of metallic and non-metallic materials can be enhanced by tailoring the surface morphology to increase multiple internal light reflections and absorption. In our earlier work, we demonstrated that multiscale fractal texturing of surfaces could lead to enhanced light trapping and photothermal conversion [9]. In the present study, we seek to systematically investigate the effect of fractal surface texturing on the absorptance of the solar selective coatings, both computationally and experimentally. While much of the research on solar selective coating development has been empirical in nature in terms of either materials or fabrication parameter study, there are scant fundamental theoretical modeling studies on explaining or understanding the underlying physics. Sound physical modeling will complement and aid the designing of surface

topographies and the development of coating materials for maximizing optical performance and will therefore be of much value in advancing CSP technologies.

Coatings fabricated using industrially versatile techniques such as electrodeposition, spray coating, or dip coating exhibit inherently rough morphological characteristics [14–16] that need to be captured accurately for theoretical modeling. Several researchers have used different standard roughness measures such as root-mean-squared (RMS) height, slope, and standard deviation to describe the morphology of such coatings [14–18]. Further, Kowalczewski et al. [19] modeled coating surface roughness using Gaussian disorder and approximated the optimal roughness parameters yielding the maximum absorption augmentation. However, the roughness measures of root-mean-squared (RMS) height, slope, and standard deviation are not unique for a surface and depend on the scan length and resolution of the measuring instrument [20–22]. As a result, such descriptions are prone to considerable uncertainty and inaccuracies.

From an optical modeling standpoint, a commonly used method for the calculation of the absorptance of solar selective coatings is that of ray tracing [23,24]. However, the light ray tracing process is based on the assumption that light travels in a straight line, which is only true when the characteristic structure dimension of the absorbing material's surface morphology, such as the period of a microstructure and the span of spontaneous fluctuation, is much greater than the wavelength of the incident light. However, since the majority of random surface fluctuations in typical materials are on the order of micrometers and close to visible light wavelength, the light ray-tracing approach is not well-suited for calculating the absorptivity of a rough surface [25].

It is evident from the foregoing discussion that the existing theoretical models of solar selective surfaces suffer from a lack of reliable surface description or appropriate modeling of the light interaction with the surface or both. The goal of this study is to address both limitations and present a physics-based computational approach to modeling the optical properties of practical, fractal-textured solar absorber surfaces and to derive surface topographies that enhance solar absorptance. To this end, a textured absorber with a multiscale morphology is represented as a fractal surface described by the Weierstrass-Mandelbrot (W-M) function [21,22], whose parameters can be obtained uniquely from a profilometric scan of an actual absorber surface without any assumed parameters. The fractal surface description is scale-invariant and overcomes the limitations of conventional measures of a rough surface [26].

A computational model for the interaction of solar radiation with the fractal surface is developed, for the first time, by solving the governing Maxwell's equation, from which the absorptance is obtained as a function of the surface fractal parameters and material properties. A systematic parametric study is presented to elucidate the effects of texturing on the solar absorptance of the coatings. The computational model is validated with experimental studies on fractal textured solar absorber coatings fabricated by electrodeposition, in which the multiscale topology is systematically varied by changing the electrodeposition parameters. The model is shown to describe the measured spectral and average absorptance of Cu, CuO, and CuMnO coatings in a unified manner. Furthermore, the thermal emittance of the deposited Cu, CuO, and CuMnO is experimentally measured. The solar absorptance is shown to increase with the fractal dimension, absorptance values as high as 0.985 is obtained through fractal surface texturing, while retaining low emittance, which demonstrates excellent solar selectivity of the developed surfaces.

The article is organized as follows: the fractal description of textured solar absorber surfaces is presented in Section 2; the mathematical description of coating and the numerical simulation details are presented in Section 3; experimental studies on fabrication and characterization of fractal textured coatings are discussed in Section 4; the results of the study are detailed in Section 5; and the key findings are summarized in Section 6.

2. FRACTAL SURFACE DESCRIPTION

Solar selective coatings fabricated using typical methods show roughness features at multiple length scales, ranging from micrometers to nanometers. Figures 1a–c shows the scanning electron microscope (SEM) images of an electrodeposited copper surface at progressively increasing magnifications. The images reveal asperities at several length scales distributed uniformly over the surface. The presence of smaller length scale asperities progressively layered on top of larger length scale asperities is noticeable with increasing magnification, indicating the fractal structure of the surface. Furthermore, asperities at smaller length scales appear with magnification, as seen in the insets of the profilometric scan of the surface presented in Figure 1d, where the magnified details of the profile are not a copy of the initial profile but a scaled one with different scaling

factors at different magnifications. Therefore, the surface profiles under study are self-affine in nature.

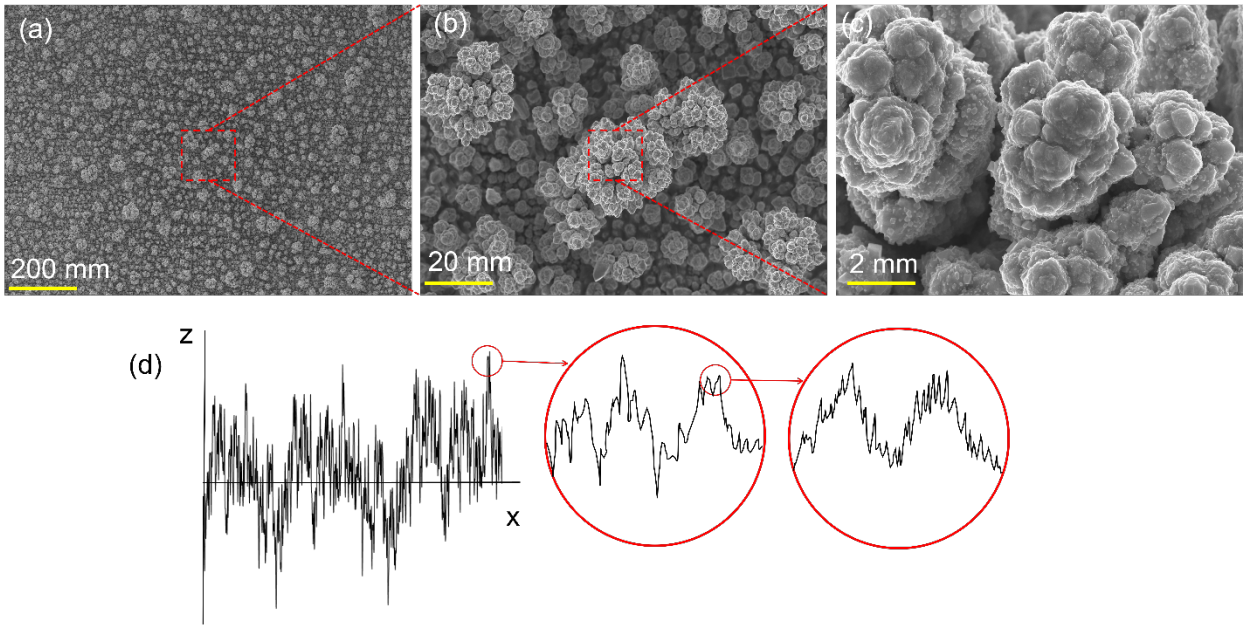

Figure 1: (a−c) SEM images of an electrodeposited coating surface at different magnifications, (d) a representative profilometric line scan of the surface revealing self-affine characteristic of smaller length scale asperities being uncovered upon repeated higher magnification,

Such a profile, $z(x)$, may be considered as a superimposition of multiple waves of different wavelengths and amplitudes at different (random) phases and may be represented by the Weierstrass-Mandelbrot (W-M) function [21,22], given below, which contains the principal characteristics of rough multiscale surfaces namely, self-similarity, non-differentiability, and continuity:

$$z(x) = G^{D-1} \sum_{n=n_1}^{\infty} \frac{\cos(2\pi\gamma^n x)}{\gamma^{(2-D)n}} \tag{1}$$

where x is the lateral distance, D is the fractal dimension, G is a scaling constant, γ^n is a frequency mode corresponding to the horizontal length-scale dimension (L) of roughness feature as $\gamma^n = \frac{1}{L}$, and $\gamma^{n_1} = \frac{1}{L_{max}}$ is the minimum (cutoff) frequency which corresponds to the maximum asperity length-scale. The parameter γ determines the relative difference between the phases of participating waves in the superimposition that defines the multiscale rough surface. Random phases require the simulation of multiscale rough surfaces to have noncoincident phases of

frequency modes. A value of $\gamma = 1.5$ ensures such noncoincident random phases of frequency modes [27].

The power spectrum of the W-M function exhibits a power-law dependence on the spatial frequency, ω, given by:

$$S(\omega) = \frac{G^{2(D-1)}}{2\ln(\gamma)} \frac{1}{\omega^{(5-2D)}} \tag{2}$$

where ω is the spatial frequency in units of m^{-1}. The power-law dependence of the power spectrum on the spatial frequency, ω, indicates the fractal nature of the W−M function. The fractal parameters of the textured surface can be obtained by a direct comparison between the power spectrum of the W−M function (Equation (2)) and the power spectrum of the textured surface profile (Figure 1d).

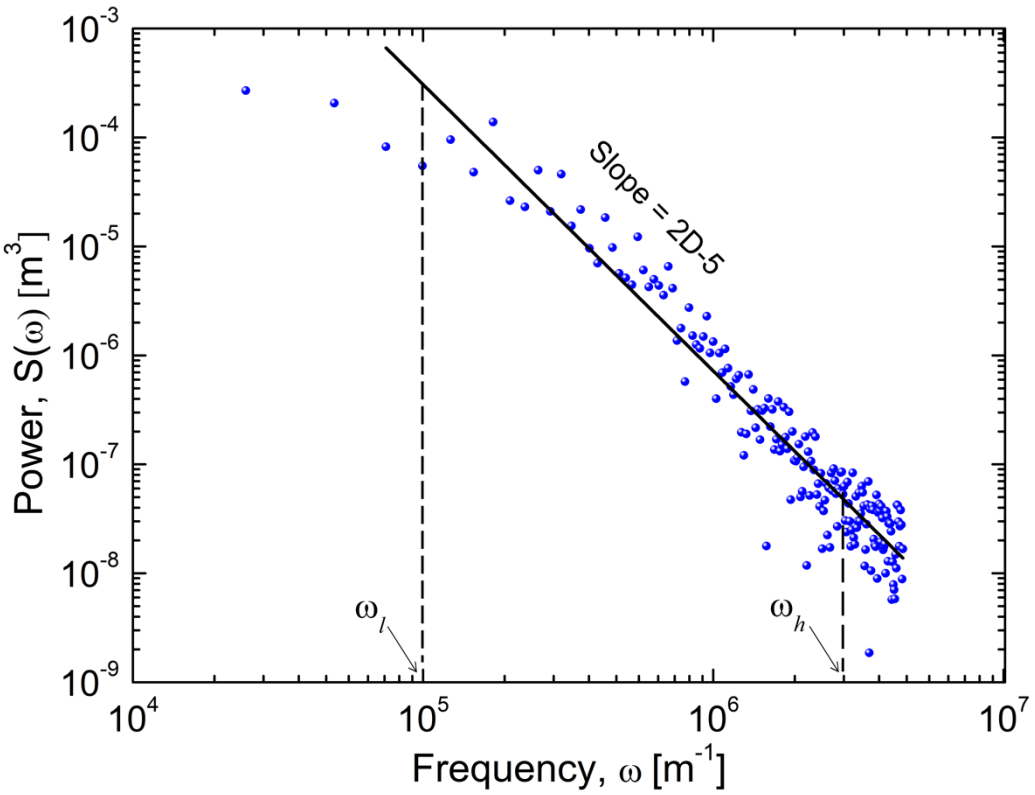

Figure 2: Fast Fourier transform (FFT) based power spectrum of the surface in Figure 1, showing the fractal characteristics of the surface over a frequency range.

Figure 2 shows one such power spectrum obtained based on the fast Fourier transform of a profilometric scan of the electrodeposited copper surface shown in Figure 1d, where the wavelengths (spatial frequencies) contributing to the power spectrum of the surface profile lie

between a minimum (ω_l) and a maximum (ω_h) value which are characteristic of the rough surface [21,22,28,29]. The lowest ($\omega_l = 10^5\ m^{-1}$) and highest ($\omega_h \approx 2.5 \times 10^5\ m^{-1}$) frequency values correspond to the maximum (L_{max}) and minimum (L_{min}) length-scales of the asperities of a rough surface, respectively, such that $L_{max} = \frac{1}{\omega_l}$ and $L_{min} = \frac{1}{\omega_h}$. Further, a linear best fit curve on a log-log plot of the power spectrum (Figure 2; $R^2 = 0.91$), compared to the power spectrum of the W-M function, gives the characteristic fractal parameters of the rough surface. The slope of the linear best fit curve in the characteristic frequency range (ω_l , ω_h) determines the fractal dimension D such that the slope equals to $(2D - 5)$, and the intercept on the power axis is used to determine the scaling constant G. Therefore, a fractal representation of a rough surface, when compared with the W-M function, uniquely determines the characteristic fractal parameters (D, G, L_{min} , L_{max}).

3. OPTICAL MODELING

Figure 3a represents the solar radiation reaching a plane surface, and a schematic representation of textured absorber surfaces described using the W-M function at three different fractal dimension values. Solar radiation (I_o) is incident on the rough coating surface, a part of which is reflected back to the ambient, and the remaining is transmitted or absorbed by the coating and the substrate. The coating reduces the reflection due to the multiscale micro-and nanostructured asperity structures, thereby absorbing more radiation for thermal conversion.

Figure 3b shows a schematic of the geometry and the domain considered in the optical modeling of the textured solar absorber surface based on the W-M function. The width (W) of the computational domain is considered to the three times of the L_{max} and the thickness of the coating is considered 3 μm based on the experimental characterization. The thickness of the substrate is considered twice the coating thickness for the simulation purpose. Light is launched from the interior port AB (dashed line) toward the material interface at a wavelength, λ, and at an angle, θ, and light reflected from the rough surface toward this port passes through the section AB and is absorbed in a top perfectly matched layer (PML). At the EF boundary in 3b, the power flux in the upward direction is integrated and normalized by the incident power of the incoming radiation $I_o(\lambda, \theta)$ to obtain the total reflectance. A boundary layer mesh at the EF boundary layer is introduced with a single layer of elements much smaller than the wavelength to determine the integral of the power flux more accurately. The PML absorbs both the propagating and evanescent

components of the field, but since only the propagating component needs to be absorbed, the PMLs should be placed far enough away from the material interfaces, and the PML should be at least half a wavelength away from the material interfaces to satisfy this condition. In the present study, the distance of the PML layer is twice the maximum wavelength considered for the study. Below the solar absorber coating is the substrate alloy onto which the coating is applied, such that the model considers the optical interaction of both the coating as well as the substrate with solar radiation. For reducing the computational domain in the simulation, only a skin of the substrate of thickness equal to twice the coating thickness was considered. The PML below the substrate (Figure 3b) absorbs all the radiation reaching the layer, thereby making the simulations valid for any realistic thickness of the substrate.

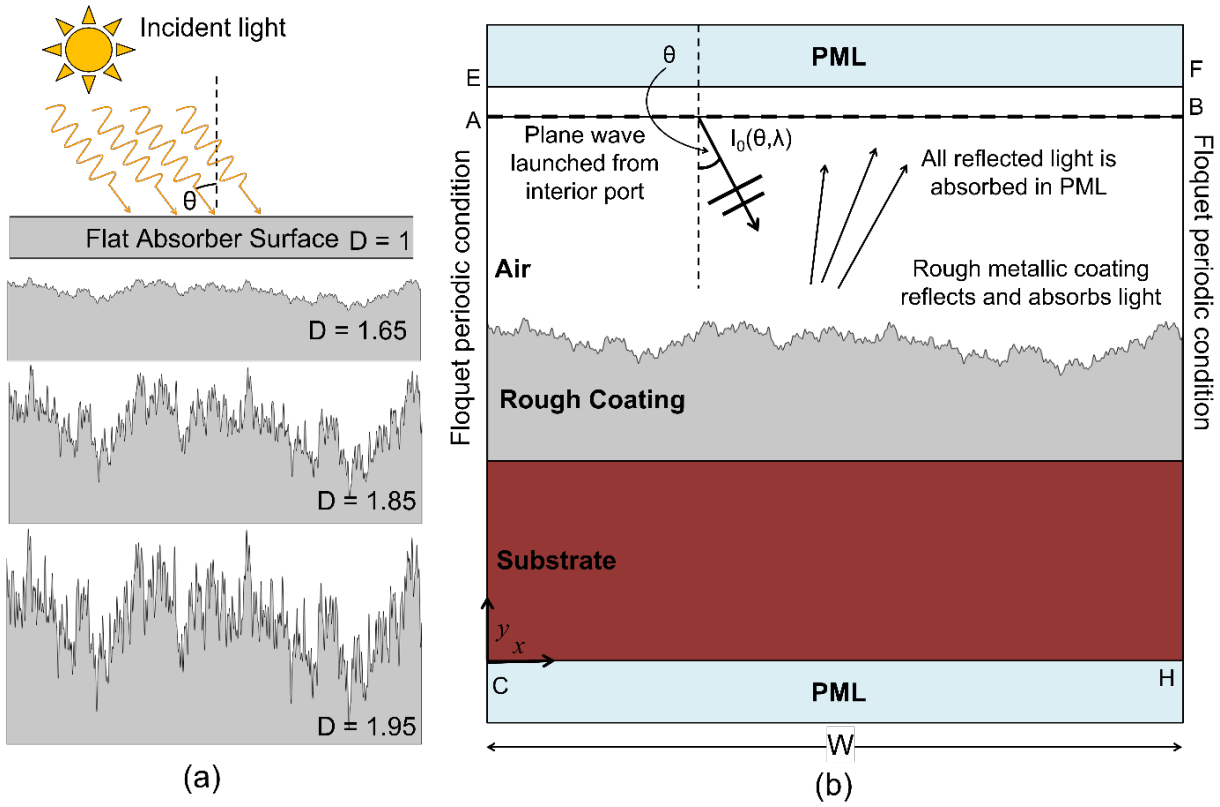

Figure 3: Description of the optical model: (a) illustration of texture absorber surfaces based on the W-M function at different fractal dimensions; (b) schematic of the computational domain.

The electromagnetic theory is used to investigate the effect of surface morphology and surface roughness on material absorptivity since an optical wave is a form of electromagnetic wave that propagates according to Maxwell's equations, which can be expressed as:

$$\nabla \times \left(\mu_r^{-1} \nabla \times \vec{E}\right) - k_0^2 (n - ik)^2 \vec{E} = 0 \tag{3}$$

where $\vec{E}$ represents the electric field, μ_r is the relative magnetic permeability (taken to be unity, μ_r = 1), k_0 is the wavenumber of free space given by $k_0 = \omega\sqrt{\varepsilon_0 \mu_0} = \omega/c_0$, in which c_0 is the speed of light in the vacuum, and $\omega = 2\pi f = 2\pi c/\lambda$ is defined by wavelength λ. The terms n and k are the real and imaginary parts of the refractive index, respectively. Spectral refractive index (n and k) for the coating materials Cu, CuO, CuMnO, and substrate material Inconel is taken from the literature [30–34].

Equation (3), subject to the boundary conditions and the incident radiation power, $I_0(\lambda, \theta)$, from the inlet port (AB), is solved for the complex electric field, $E(x, y, \lambda, \theta)$, from which the three-dimensional field is obtained in terms of the out-of-plane wave number k_z as:

$$E(x, y, z, \lambda, \theta) = \tilde{E}(x, y, \lambda, \theta) e^{-ik_z z} \tag{4}$$

in which $\tilde{E}(x, y, \lambda, \theta)$ is the complex amplitude. The irradiance (power density) is obtained from the electric field using the relationship [35]:

$$I(x, y, z, \lambda, \theta) = \frac{1}{2} n \sqrt{\frac{\varepsilon_0}{\mu_0}} \left|\vec{E}\right|^2 \cos\theta \tag{5}$$

in which ε_o and μ_o are the permittivity and permeability of free space, $\left|\vec{E}\right|$ is the magnitude of the electric field, and θ is the incidence angle. The reflectance at the glass surface, $R(\lambda, \theta)$, can be calculated as the ratio of the power flow in the positive y-direction (reverse to the launch of the plane wave) to the base power $I_0(\lambda, \theta)$ at the boundary EF in Figure 3b. The absorptance is then determined from the reflectance as $\alpha(\lambda, \theta) = 1 - R(\lambda, \theta)$. The spectral reflectance, $R(\lambda)$, is obtained by integrating $R(\lambda, \theta)$ over θ. from which the spectral absorptance is determined as $\alpha(\lambda) = 1 - R(\lambda)$, and, likewise, by integrating $R(\lambda, \theta)$ with respect to λ over the relevant wavelength range and taking its 1's complement, the average absorptance variation with the incidence angle, $\bar{\alpha}(\theta)$, is obtained.

The governing partial differential equations subjected to the boundary conditions were solved using the Wave Optics, Electromagnetic Wave, and Frequency Domain modules of the commercial software COMSOL Multiphysics 5.5, based on the finite element method [36] software based on the finite element analysis technique. The computational domain was discretized appropriately, and the mesh size dependency was studied to determine the size based on accuracy and computation time. A mesh refinement study was conducted by progressively reducing the

mesh size in the computation domain until decreasing the mesh element size further yielded no significant change in the results. The mesh element size was reduced near the coating boundary and air to minimize the error in the calculations. To guarantee the accuracy of the solution, the biggest mesh dimension is less than $\frac{\lambda_0}{6n}$, where λ_0 represents the incident light minimum wavelength, and n is the refractive index of the medium. The equations were solved in the electromagnetic wavelength domain with the wavelength sweep and stationary solver in COMSOL Multiphysics 5.5, having relative tolerance of 10^{-4}.

4. EXPERIMENTAL METHODS

4.1. Coatings Fabrication

Durable absorber coatings of CuO and CuMnO were fabricated on Inconel 625 substrates by electrodeposition [9,37–39], using an AUTOLAB PGSTAT128N potentiostat (ECO Chemie, Utrecht, The Netherlands). The setup consisted of a three-electrode system with the working electrode, reference electrode and counter electrode selected based on the substrate on which the coating is desired. As described in our patents, the coating parameters were selected to generate fractal textured surfaces [37,38].

For fabrication of CuO coatings, a Cu coating was first deposited on Inconel 625 substrate from an aqueous electrolyte solution containing $CuSO_4$(1M) and H_2SO_4 (0.5M). The three-electrode system consisted of a platinum mesh as a counter electrode, Ag/AgCl as a reference electrode, and Inconel 625 substrate with an exposed area of 12.25 cm^2 as the working electrode. The solution was deaerated by bubbling it with nitrogen for 15 min prior to the fabrication of each sample. All the electrodes were rigorously cleaned with acetone, methanol, and deionized water to remove any dirt and grease from their surfaces and dried in air. Electrodeposition was performed over a range of voltages from 0.7 V to 1.3 V, followed by the application of a low overpotential for a short duration after deposition [9,37,39]. After electrodeposition, the surfaces were rinsed with acetone and deionized water and dried with nitrogen gas. The deposited Cu coating was then annealed at 500 ^oC for 2 hours in the air in a box furnace for the preparation of a black CuO absorber.

Copper manganese oxide (CuMnO) films were deposited on Inconel 625 substrate from an aqueous solution containing 0.05M of copper nitrate, manganese nitrate, and 0.1M potassium

nitrate; the solution was stirred at 200 rpm for one hour. Copper (II) nitrate trihydrate (99%, ACROS ORGANIC), Manganese (II) nitrate tetrahydrate (98%, Alfa Aesar), and Potassium nitrate (99%, Alfa Aesar) was used as precursor materials [38]. The three-electrode system was 15 cm^2 platinum mesh as a counter electrode, Ag/AgCl as a reference electrode, and a metal substrate sheet with an exposed area of 12.25 cm^2 as the working electrode. The substrate was rigorously cleaned in an ultrasound cleaner with deionized water, acetone, and 2-propanol to remove dirt and grease from their surfaces and dry in the air. The electrodeposition allowed for a range of overpotentials from 0.9 V to 1.3 V. After deposition, coatings were annealed at 500 °C in an air furnace for 2 hours to form black-colored CuMnO coatings [38].

4.2. Microstructural and Optical Characterization

Field emission scanning electron microscopy (FESEM, Model LEO-Zeiss FESEM) was used to study the morphology of the coatings; images were taken at different magnifications to study the multiscale structures developed during electrodeposition.

A Zygo NewView 8000 series three-dimensional optical surface profiler was used to perform profilometric measurements on the prepared solar selective coatings. The instrument uses coherence scanning interferometry to measure the surface profile and provide non-contact, highly accurate and quick measurements of the prepared surfaces. Surface profile scans were performed at three different locations for each sample. The measured profile scan data was analyzed using the image and surface analysis software Gwyddion [40] and Matlab to obtain its averaged Fourier transform-based power spectrum. Using the obtained power spectra for the individual surfaces, their corresponding fractal parameters were calculated as described in Section 2.

Spectral total absorptance, $\alpha(\lambda)$ $(= 1 - R(\lambda))$, of the absorber coatings was recorded with a Cary 5000 UV-Vis-NIR spectrophotometer equipped with an integrating sphere. Measurements were recorded in the 300 to 1500 nm wavelength range. A PTFE reflectance standard was used to calibrate the instrument before the actual measurement. The average solar absorptance of the coatings was measured using a solar spectrum reflectometer (Model SSR) of Devices and Services, as per ASTM G173 standard. For the solar spectrum reflectometer, the illumination source was a tungsten-halogen lamp. The radiation reflected by the sample is measured at an angle of 20° from the normal, with four filtered detectors (UV, blue, red, and infrared). A solar spectrum measurement was achieved by adding the four outputs in the appropriate proportions. The solar spectrum reflectometer was calibrated using a standard sample.

5. RESULTS AND DISCUSSION

The computational model presented in Section 3 was utilized to simulate the optical properties of fractal textured absorber surfaces. The results of the study are discussed in this section, first elucidating the effect of the fractal parameters on the spectral and average reflectance and absorptance in Section 5.1. The morphological, fractal, and optical characterization of the different fractal textured coatings fabricated in the experiments are then discussed in Section 5.2. The computational modeling of the optical properties of the fabricated coatings are compared to the experimental measurements in Section 5.3.

5.1. Effects of Fractal Texturing on the Optical Properties

Figure 4 presents the spectral variation of the reflectance of electrodeposited CuMnO coatings over wavelengths ranging from 350 nm to 1100 nm at different light incidence angles, θ = 0° (normal incidence), 30°, 45°, 60°, and 75°, for nine combinations of fractal dimension, D, and scaling factor, G, of the W-M function. The reflectance of the absorber surface increases with an increase in the light incidence angle for all D and G values. An increase in the incidence angle corresponds to increasing deviation from normal incidence, thereby increasing the reflected component compared to the absorbed component of the radiation. In the limit of $\theta = 90°$, corresponding to grazing incidence, all the incident radiation is reflected regardless of wavelength for the reflectance of unity. The variation of the spectral reflectance profiles with an angle in Figure 4 confirms this trend.

The effect of increasing fractal dimension D on the spectral reflectance is seen in the plot frames Figures 4(a-c), (d-f), and (g-i) going from left to right, in each of the three rows representing a different scaling factor G. An increase in the fractal dimension, D, denotes an increase in the surface roughness, which enhances light trapping in between the asperities. As a result, the reflectance over the fractal-textured absorber surface decreases. For an increase in fractal dimension from 1.65 to 1.95, the reflectance is seen to decrease by two orders of magnitude for all values of the scaling constant, G, and incidence angle, θ.

Figure 4 further shows that the reflectance decreases with an increase in the scaling factor G, because the asperity height increases with G, which, in turn, enhances the light trapping. For the small D value, nearly linear trends are observed (Figure 4a, d, and g), and with an increase in the scaling factor G as well as D, the variation of spectral reflectance shows nonmonotonic variation

with wavelength due to the interactions of the different wavelengths with the different asperity sizes. Compared to the effect of the fractal dimension, increasing the scaling factor offers a modest reduction in the reflectance by a factor of 2-4. Overall, Figure 4 shows that the reflectance may be dramatically reduced by tailoring the fractal dimension and the scaling constant. For example, the reflectance values range from about 0.2 for $D = 1.65$ and $G = 1\ \mu m$, and reduce to about 0.001 for $= 1.95$ and $G = 2\ \mu m$. It is also important to observe that a two-order reduction in reflectance through absorber surface texturing is achieved for high incidence angles as well. The results point to significant opportunities for solar radiation capture over a wider range of incidence angles through fractal texturing.

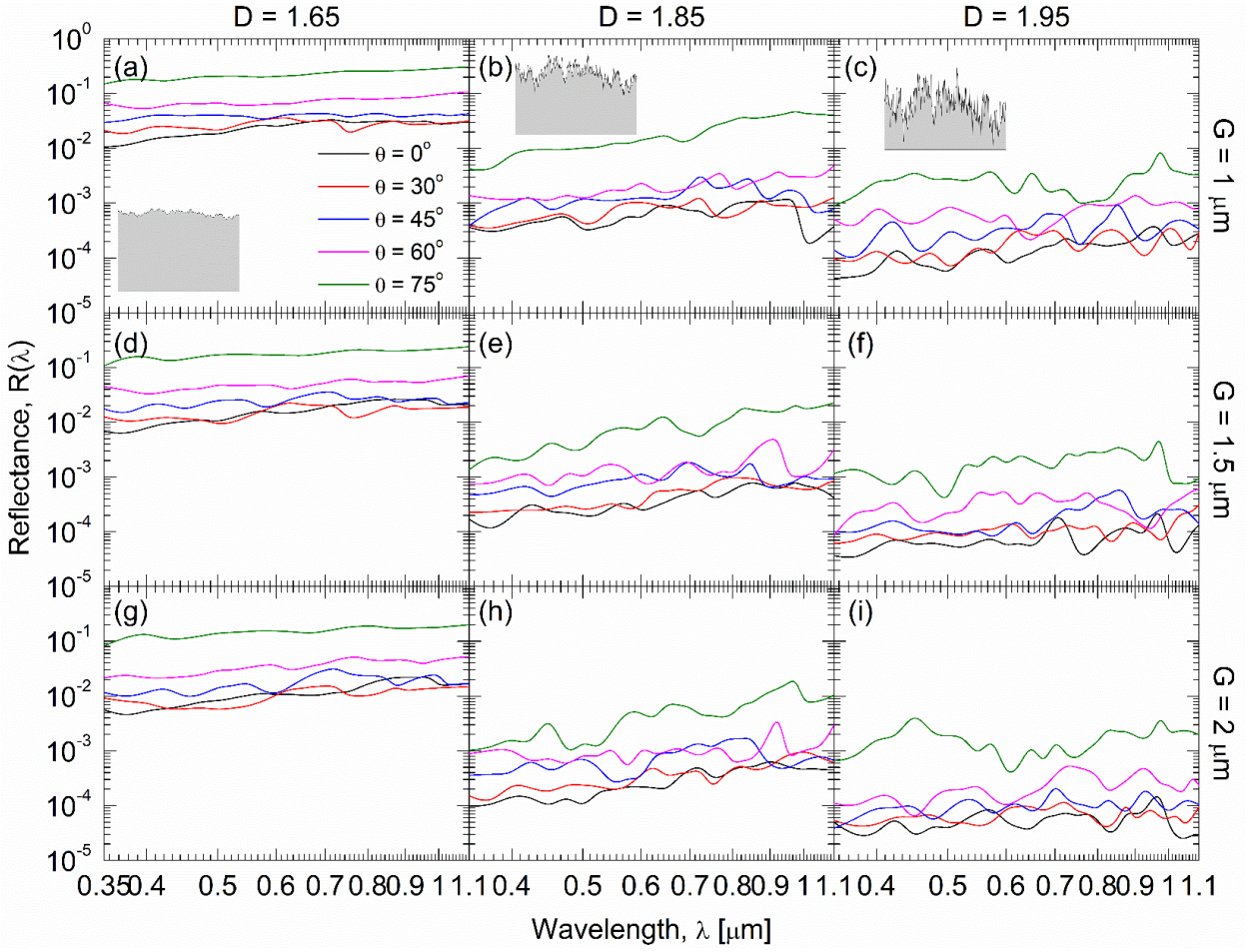

Figure 4: Spectral variation of reflectance of CuMnO coatings at different incidence angles, for various combinations of fractal dimension, D, and scaling constant, G.

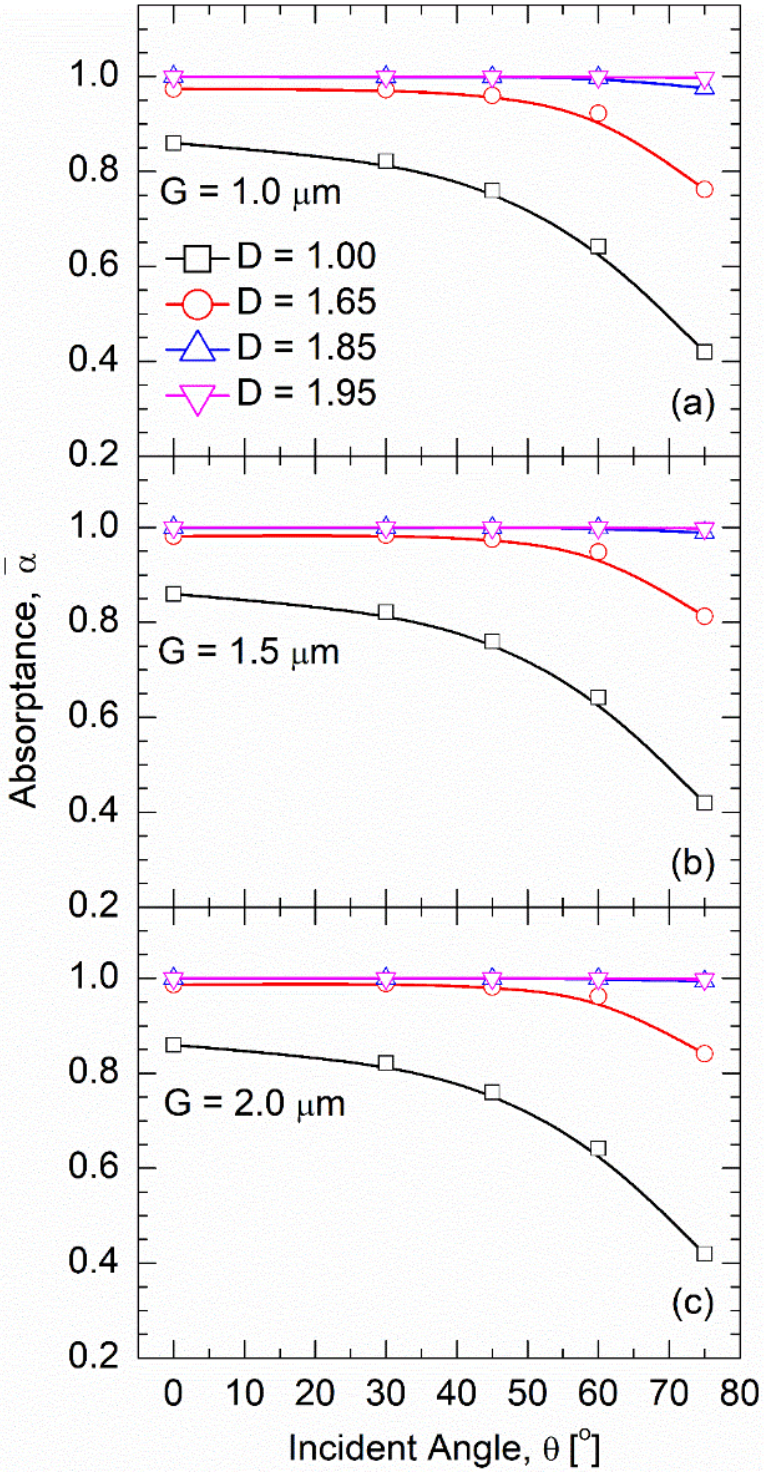

Figure 5: Variation of spectrally averaged absorptance with incidence angle for different combinations of fractal dimension, D, and scaling constant, G.

Figure 5a-c represents the variation of the spectrally averaged absorptance with incidence angle θ for absorber surfaces with different fractal dimensions D, and scaling constant, $G = 1\ \mu m$

(Figure 5a), 1.5 μm (Figure 5b) and 2 μm (Figure 5c). The spectrally averaged absorptance was calculated by first spectrally averaging the reflectance profile to obtain $R(\theta)$, and then taking its 1's complement to obtain $\bar{\alpha}(\theta)$. For a given fractal surface, the absorptance is nearly unity for normal incidence of light ($\theta = 0°$) and decreases with an increase in θ; when the light wave is parallel to the surface ($\theta = 90°$), no component is absorbed by the surface. It is seen that with increasing fractal dimension from that of a plain surface, the absorptance increases significantly. Beyond a certain fractal dimension, $D \approx 1.85$ in Figure 5, the absorptance value saturates as it is already near unity, as seen by the overlapping curves for $D = 1.85$ and 1.95 for all G values. Further, it is noted from Figure 5 that the absorptance is about 1 over a wide range of incident angles than the plain surface. This range increases with increasing fractal dimension, D, and/or the scaling constant, G. For example, the absorptance stays near 1 for $\theta < 65°$ in Figure 5 for $D = 1.85$ and 1.95, whereas for the untextured surface ($D = 1$), the decrease in absorptance is pronounced for all values of θ starting from 0°. Similarly, as G increases (for a given fractal dimension), the range of incidence angle over which the absorptance remains nearly constant increases. As an illustration, considering $D = 1.65$, the incidence angle range extends till 47.5° for $G = 1\ \mu m$ (Figure 5a), 52.5° for $G = 1.5\ \mu m$ (Figure 5b), and 57.5° for $G = 2\ \mu m$ (Figure 5c).

Overall, Figures 4 and 5 point to the significant benefits of fractal texturing in increasing solar energy absorption and, further, that the absorption characteristics can be tailored through appropriate texturing to obtain the desired fractal parameters.

5.2. Fractal Morphology of CuO and CuMnO Coatings

Fractal-textured CuO and CuMnO coatings were prepared via electrodeposition, as described in Section 3. The theoretical studies presented in Section 4 point to the ability to tailor the absorptance based on the topology of the fractal texturing, which can be adjusted by means of the electrodeposition overpotential. To this end, the impact of the applied overpotential on the morphologies of CuO and CuMnO-based solar selective coatings were systematically investigated.

Figure 6 shows the SEM images of CuO samples deposited at overpotentials of 0.7 V (Figure 6a,b), 0.9 V (Figure 6c,d), and 1.1 V (Figure 6e,f), each at two different magnifications. The fabricated CuO coatings demonstrate randomly rough morphologies with progressively increasing hierarchical asperity structures at multiple scales, with increasing deposition voltage. The images at 0.7 V show incipient rough textures that are homogeneously distributed on the surface. The

magnified image shows globular asperity structures with minimal depth to the features. With increasing voltage to 0.9 V, a more intricate network of multiscale asperity structures is seen to evolve, and at 1.1 V, a complex three-dimensional network of the multiscale textured surface is evident with the presence of multiple internal reflection surfaces for enhanced light capture.

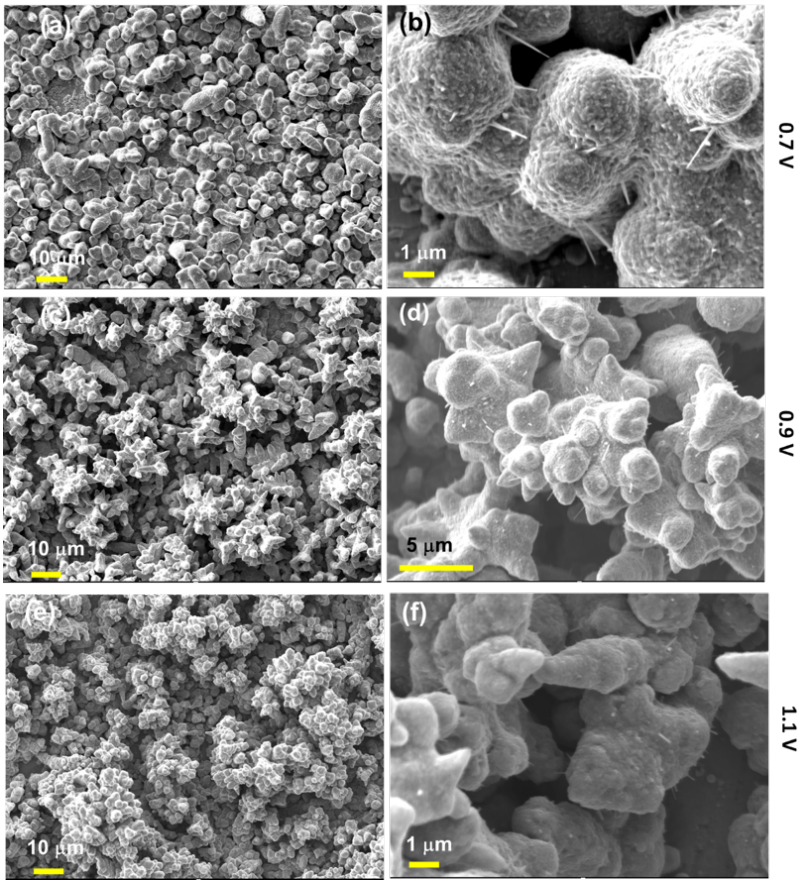

Figure 6: SEM images at two different magnifications showing the morphologies of electrodeposited CuO coatings fabricated at (a,b) 0.7 V, (c,d) 0.9 V and (e,f) 1.1 V.

Similarly, Figure 7 shows the scanning electron micrographs of CuMnO coatings deposited at overpotentials of 0.9 V, 1.0 V, and 1.1 V, each at three different magnifications. For CuMnO coatings, at lower voltages, just a few micrometer-sized, island-like particles form on the substrate surface, as seen in Figures 7(a-c). At a deposition voltage of 1.0 V, the microclusters formed at lower voltages begin branching in coatings, as seen in Figure 7(d-f). CuMnO coatings deposited at 1.1V, on the other hand, have a distinct multiscale, multi-layered structure (Figure 7(g-i)) with compact micro-sized layers at the top (Figure 7(g)) and nano flower-like structures at the bottom (Figure 7(i)). The low magnification image in Figure 7(g) shows that these micro-features are interconnected and formed clusters, leaving a few micro gaps between them that act as light traps.

The cascade of texture features from the micro-sized top layers to the nano-sized flowers at the bed of the asperities makes the textured surface required for a perfect solar absorber.

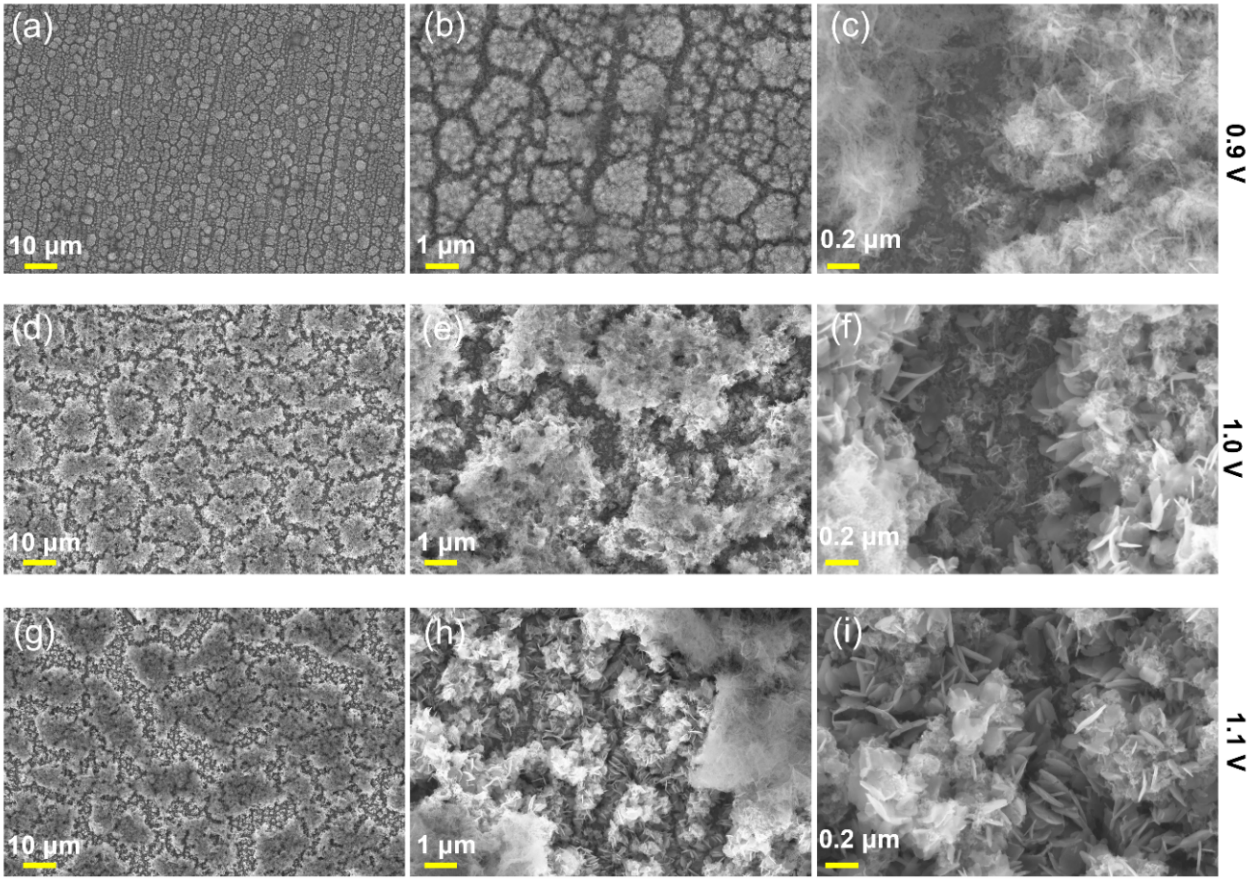

Figure 7: SEM images at three different magnifications showing the morphologies of electrodeposited CuMnO coatings fabricated at (a,b,c) 0.9 V, (d,e,f) 1.0 V and (g,h,i) 1.1 V.

It is clear from Figures 6 and 7, therefore, that tailored multiscale structures with a significant fractal component may be fabricated through proper selection of the fabrication parameters. Figure 8 examines the fractal nature of the textured surfaces quantitatively in terms of the variation of the fractal dimension of CuO and CuMnO coatings fabricated with increasing deposition voltages. For both coatings, the fractal dimension is seen to increase from about 1.6 for deposition at the smaller voltage to about 1.93 at the higher voltages. The fractal dimension for CuO coating deposited at 0.7 V is 1.66, but as the deposition voltage increased, the fractal dimension increased from 1.88 for 0.9 V to about 1.92 for 1.1V and remained near that level for coatings deposited at 1.3 V. Similarly, the fractal dimension of the deposited CuMnO coatings also increased with an increase in the deposition voltage: at the deposition voltage values of 0.9 V, 1.0 V, 1.1 V, and 1.3 V, the corresponding fractal dimension values are 1.7, 1.8, 1.9, and 1.92.

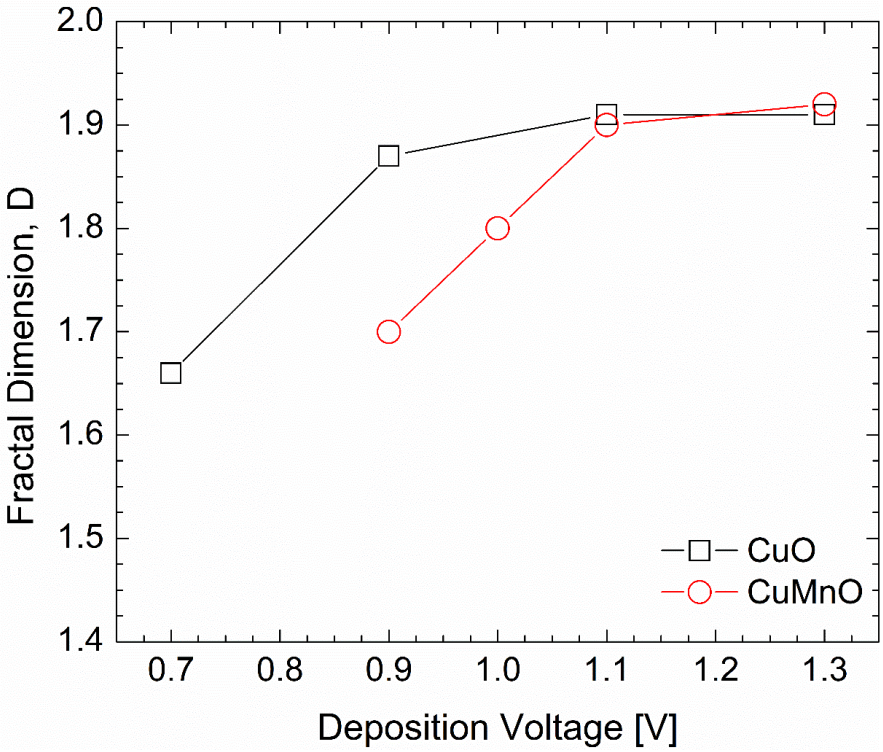

Figure 8: Variation of the fractal dimension of CuO and CuMnO surfaces electrodeposited at various voltages.

In both coatings, significant growth in fractal texturing is seen for deposition voltage up to 1.1V, as seen in the SEM images in Figures 6 and 7, as well as in the fractal dimension values in Figure 8. Beyond about 1.1 V, the fractal texturing remains more or less the same, as seen in Figure 8. Fractal dimensions close to the maximum value of 2 for the coatings prepared at overpotentials above 1.1 V demonstrate the highly fractal nature of the surfaces prepared at the high overpotentials. During electrodeposition, a high degree of morphological instability is formed in the deposits generated at the higher overpotentials due to a smaller growth time constant associated with these processing conditions, which leads to the aggressive fractal texturing on the absorber surfaces [37,38]. Overall, the measured fractal dimension values correlate closely to the observed features in the SEMs in Figures 6 and 7, confirming the validity of fractal dimension as an apt quantitative measure of the surface textures.

5.3. Comparison of Experimental and Simulation Results

The computational model developed in Section 3 was used to simulate the spectral reflectance, $R(\lambda)$, and spectral average absorptance ($\bar{\alpha}$) of the different fractal-textured coatings discussed in Section 5.2 as well as surfaces from the literature and compared to the respective experimental

measurements. Figure 9 compares measured and simulated spectral reflectance (Figure 9a) as well as average spectral absorptance (Figure 9b) variation for plain untextured copper (Cu), fractal-textured copper electrodeposited at 1.1 V, and 1.1 V electrodeposited and heat-treated copper-oxide (CuO) coatings over the wavelength ranging from 300 nm to 1100 nm. The experimental data for the different surfaces were obtained from Jain and Pitchumani [9]. The fractal dimension D for the electrodeposited copper and CuO is obtained from Figure 8 as 1.92 corresponding to a deposition voltage of 1.1 V, and the coating thickness is 3 μm. The data for the real and imaginary parts of the refractive index (n and k) for bare Cu and CuO were taken from Rakić et al. [41] and Özer et al. [42].

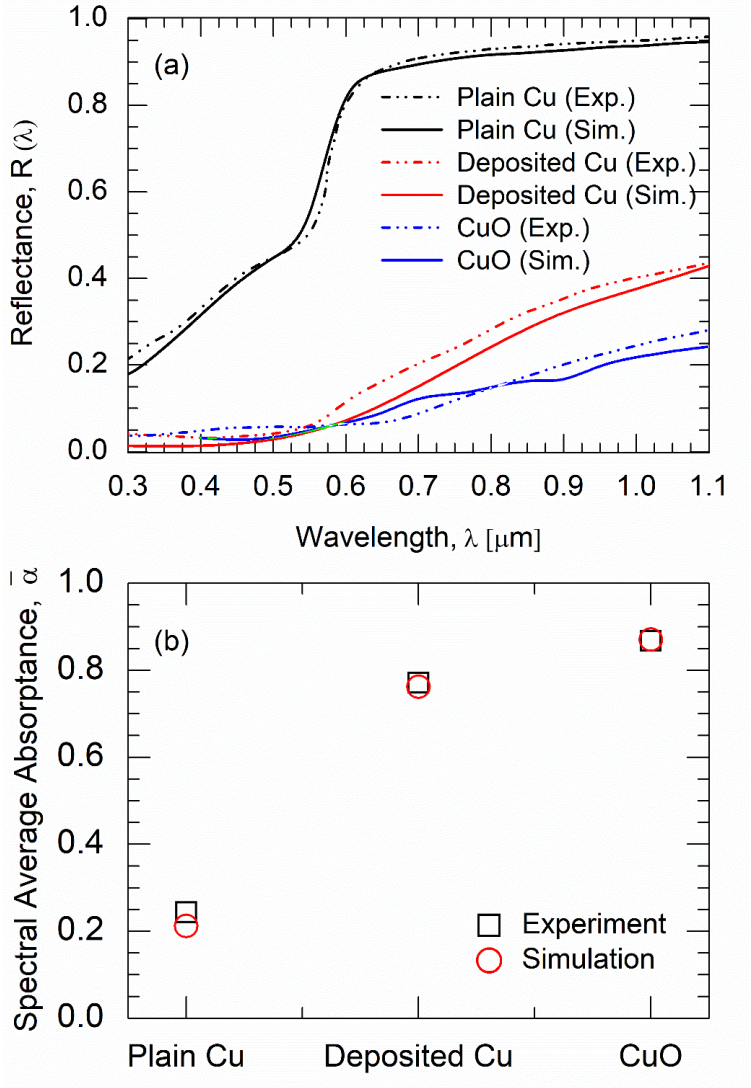

Figure 9: Comparison of experimental and simulation results: (a) spectral variation of reflectance and (b) spectral average absorptance.

Figure 9a shows that the reflectance of plain untextured Cu is high (black lines), which is reduced substantially by fractal surface texturing (red lines). Heat treatment of the deposited Cu coatings creates a black oxide, CuO, which further reduces the reflectance (blue lines). In all the cases, the simulated reflectance values follow the measured spectra closely over the entire wavelength range considered. Further, Figure 9b presents the spectral average absorptance of the plain untextured Cu, electrodeposited, fractal-textured Cu, and fractal-textured CuO coatings. The measured and simulated spectral average absorptance for plain Cu, fractal-textured Cu and fractal-textured CuO are 0.24, 0.77, and 0.86 (measured) and 0.21, 0.76, and 0.87 (simulated), respectively, which demonstrates an excellent agreement between the physics-based simulations and the experimental measurements for all Cu based coatings. The measured thermal emittance of deposited Cu and CuO ranged from 0.15 to 0.66 at the deposition voltage from 0.3 V to 1.1 V [9].

Following the same format as in Figure 9, Figure 10 compares the measured and simulated spectral reflectance (Figure 10a) and spectral average absorptance (Figure 10b) of CuMnO coatings over a range of electrodeposition voltage and, in turn, fractal dimensions as provided in the legend of Figure 10a. For plain untextured CuMnO coating, the experimental measurements were taken from Falahatgar et al. [33], while for all other textured coatings, the measurements were conducted in this study as discussed in Section 4.2. The numerical simulation for the fractal textured CuMnO coatings was conducted based on the fractal characterization of the deposited CuMnO solar selective coatings presented in the previous section: the fractal dimension for deposited CuMnO at 0.9 V, 1.0 V, 1.1 V, and 1.3 V are 1.7, 1.8, 1.9, 1.92, respectively. The refractive index values with wavelength were taken from [30–34], and the measured coating thickness of 3 μm was used in the numerical simulations.

The measured thermal emittance of CuMnO ranged from 0.15 to 0.50 at the deposition voltage from 0.3 V to 1.3 V. The optimized CuMnO, which was deposited at 1.1V, exhibits an emittance of only 0.41. In comparison, even in pristine conditions, black absorber coatings applied using alternative techniques, such as spray deposition, are reported to exhibit emittance greater than 0.8 [43,44].

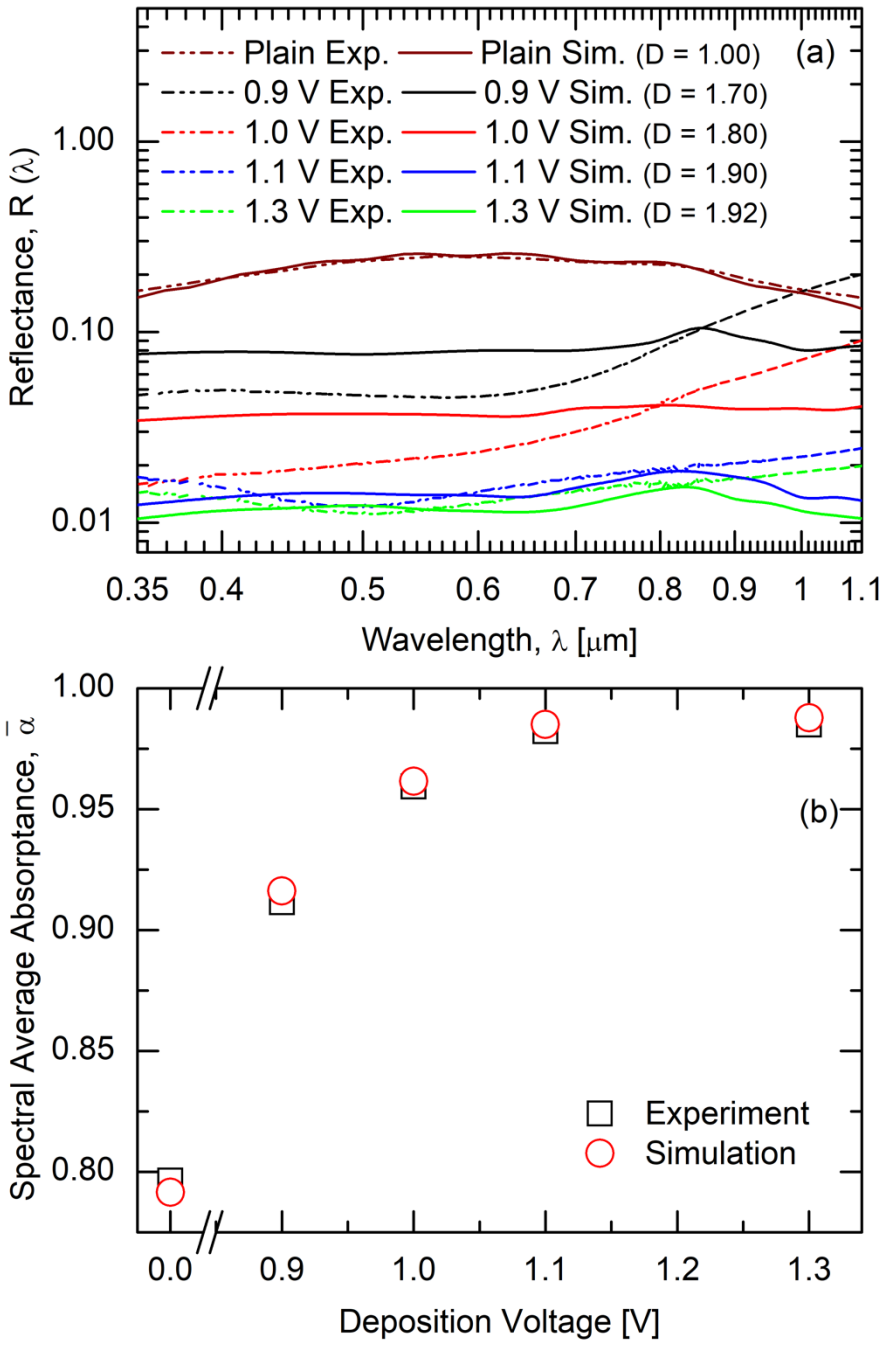

Figure 10: Comparison of experimental and simulation: (a) spectral variation of reflectance (b) spectral average absorptance.

Figure 10a compares experimentally measured and numerically simulated spectral reflectance profiles for CuMnO over the wavelength range of 350 nm to 1100 nm. The measured and simulated variations are in general agreement and follow the correct trend that the reflectance decreases with increasing fractal texturing. The differences between the simulated and measured profiles are

attributed to the variabilities in the reported refractive index values, n, and k. A further comparison is presented in Figure 10b in terms of the spectral average absorptance variation with the electrodeposition voltage. It was seen in Figure 7 that increasing voltage led to more multiscale features on the coatings, which corresponded to increasing fractal dimension value (Figure 8). Figure 10b reveals the increasing absorptance with respect to the fractal texturing achieved by the increasing deposition voltage, ranging from $\bar{\alpha} \approx 0.8$ for a plain, untextured surface to $\bar{\alpha} \approx 0.985$ for an electrodeposition voltage of 1.1 V. The results point to the effect of fractal texturing that leads to an extremely high absorptance value of much significance to Gen3 CSP applications. Furthermore, Figure 10b shows that the numerically simulated values of $\bar{\alpha} = 0.791$, 0.916, 0.961, 0.985 and 0.987 match the measured spectral average absorptance values of 0.796, 0.911, 0.959, 0.982, and 0.985 for the plain [33] and the increasingly fractal textured CuMnO solar selective coatings.

The results presented in this section demonstrate that fractal textured surfaces considerably improve the absorptance (from 0.2 to 0.985 for CuMnO, for example). At the same time, the thermal emittance of these surfaces increases only modestly (from 0.15 to 0.50 for CuMnO), which demonstrates the exceptional solar selective characteristic of the surface. The enhanced performance of the coatings would contribute to increased efficiency and reduced cost of the CSP system. The present article focused on the modeling of the absorptance of the fractal textured surfaces. Simulation of the thermal emittance requires the spectral refractive index, n and k, in the long wavelength (infrared) range, which is not available. Therefore, the modeling considered only absorptance, which is of greater significance for the air-stable absorber coatings needed for power tower applications at the Gen3 CSP temperature. Although the coatings are developed for open-air power tower applications, these can also be used for evacuated tubes. If the refractive index profiles were available in the longer wavelength range, the modeling methodology for the emittance remains the same as that presented in this article and may be pursued in a future study.

6. CONCLUSIONS

This study presented a novel approach to enhancing the solar absorptance of thermal receivers through fractal textured solar selective coatings. Representing the textured absorber surfaces as a Weierstrass-Mandelbrot function, a physics-based simulation model was developed for the first time by solving Maxwell's equations for the interaction of solar radiation with fractal surfaces.

Systematic studies were presented to elucidate the effects of the fractal parameters on spectral reflectance and spectral averaged absorptance. It was shown that fractal texturing enhances light trapping, thereby reducing reflectance and increasing absorptance compared to untextured surfaces, and yields high absorptance over a wider range of incident angles. The parametric study demonstrated that high absorptance could be achieved by tailoring the fractal parameters appropriately. Experimental studies were presented to demonstrate this finding by fabricating fractal textured solar selective surfaces of CuO and CuMnO via electrodeposition, which provided for tailoring the fractal dimension by adjusting the deposition voltage. Morphologies of the deposited coatings showed increasing fractal texturing with increasing deposition voltage. Optical measurements demonstrated a corresponding increase in the absorptance with fractal texturing with absorptance as high as 0.985 for fractal textured CuMnO. The numerical simulation model was shown to agree well with measured spectral reflectance and average spectral absorptance for Cu, CuO, and CuMnO coatings over a range of fractal texturing. The findings of the study provide fundamental insight through physics-based simulations into designing fractal-textured, high absorptance solar selective coatings and through the experimental fabrication studies a means of fabricating such surfaces for use in high-temperature solar thermal applications.

ACKNOWLEDGMENT AND DISCLAIMER

This material is based upon work supported by the US Department of Energy's Office of Energy Efficiency and Renewable Energy (EERE) under the Solar Energy Technologies Office Award Number DE-EE0008537. The views expressed herein do not necessarily represent the views of the US Department of Energy or the United States Government.

REFERENCES

[1] M. Caccia, M. Tabandeh-Khorshid, G. Itskos, A.R. Strayer, A.S. Caldwell, S. Pidaparti, S. Singnisai, A.D. Rohskopf, A.M. Schroeder, D. Jarrahbashi, T. Kang, S. Sahoo, N.R. Kadasala, A. Marquez-Rossy, M.H. Anderson, E. Lara-Curzio, D. Ranjan, A. Henry, K.H. Sandhage, Ceramic–metal composites for heat exchangers in concentrated solar power plants, Nature. 562 (2018) 406–409. https://doi.org/10.1038/s41586-018-0593-1.

[2] L. Huaxu, W. Fuqiang, Z. Dong, C. Ziming, Z. Chuanxin, L. Bo, X. Huijin, Experimental investigation of cost-effective ZnO nanofluid based spectral splitting CPV/T system,

Energy. 194 (2020) 116913. https://doi.org/10.1016/j.energy.2020.116913.

[3] R. Pitz-Paal, Concentrating solar power: Still small but learning fast, Nature Energy. 2 (2017) 17095. https://doi.org/10.1038/nenergy.2017.95.

[4] G. Schellekens, A. Battaglini, J. Lilliestam, J. McDonnell, A. Patt, 100% renewable electricity: A roadmap to 2050 for Europe and North Africa, PricewaterhouseCoopers. (2010). http://pure.iiasa.ac.at/id/eprint/9383/.

[5] M.M. Hand, S. Baldwin, E. DeMeo, J.M. Reilly, T. Mai, D. Arent, G. Porro, M. Meshek, D. Sandor, Renewable electricity futures study. volume 1. exploration of high-penetration renewable electricity futures, National Renewable Energy Lab.(NREL), Golden, CO (United States); (2012).

[6] R. Sioshansi, P. Denholm, The Value of Concentrating Solar Power and Thermal Energy Storage, IEEE Transactions on Sustainable Energy. 1 (2010) 173–183. https://doi.org/10.1109/TSTE.2010.2052078.

[7] K. Nithyanandam, R. Pitchumani, Cost and performance analysis of concentrating solar power systems with integrated latent thermal energy storage, Energy. 64 (2014) 793–810. https://doi.org/10.1016/j.energy.2013.10.095.

[8] K. Kant, P.H. Biwole, I. Shamseddine, G. Tlaiji, F. Pennec, F. Fardoun, Recent advances in thermophysical properties enhancement of phase change materials for thermal energy storage, Solar Energy Materials and Solar Cells. 231 (2021) 111309. https://doi.org/10.1016/j.solmat.2021.111309.

[9] R. Jain, R. Pitchumani, Fabrication and characterization of multiscale, fractal textured solar selective coatings, Solar Energy Materials and Solar Cells. 172 (2017) 213–219. https://doi.org/10.1016/j.solmat.2017.07.009.

[10] A. Cuevas, L. Martínez, R. Romero, E.A. Dalchiele, R. Marotti, D. Leinen, J.R. Ramos-Barrado, F. Martin, Electrochemically grown cobalt-alumina composite layer for solar thermal selective absorbers, Solar Energy Materials and Solar Cells. 130 (2014) 380–386. https://doi.org/10.1016/j.solmat.2014.07.041.

[11] T.K. Kim, B. VanSaders, J. Moon, T. Kim, C.-H. Liu, J. Khamwannah, D. Chun, D. Choi, A. Kargar, R. Chen, Z. Liu, S. Jin, Tandem structured spectrally selective coating layer of copper oxide nanowires combined with cobalt oxide nanoparticles, Nano Energy. 11 (2015) 247–259. https://doi.org/10.1016/j.nanoen.2014.10.018.

[12] A. Antonaia, A. Castaldo, M.L. Addonizio, S. Esposito, Stability of W-Al2O3 cermet based solar coating for receiver tube operating at high temperature, Solar Energy Materials and Solar Cells. 94 (2010) 1604–1611. https://doi.org/10.1016/j.solmat.2010.04.080.

[13] O. Raccurt, A. Disdier, D. Bourdon, S. Donnola, A. Stollo, A. Gioconia, Study of the Stability of a Selective Solar Absorber Coating under Air and High Temperature Conditions, Energy Procedia. 69 (2015) 1551–1557. https://doi.org/10.1016/j.egypro.2015.03.107.

[14] E. Barrera, F. Gonzalez, E. Rodriguez, J. Alvarez-Ramirez, Correlation of optical properties with the fractal microstructure of black molybdenum coatings, Applied Surface Science. 256 (2010) 1756–1763. https://doi.org/10.1016/j.apsusc.2009.09.108.

[15] M. Farooq, Z.H. Lee, Computations of the optical properties of metal/insulator-composites for solar selective absorbers, Renewable Energy. 28 (2003) 1421–1431. https://doi.org/10.1016/S0960-1481(02)00033-2.

[16] K. Xu, M. Du, L. Hao, J. Mi, Q. Yu, S. Li, A review of high-temperature selective absorbing coatings for solar thermal applications, Journal of Materiomics. 6 (2020) 167–182. https://doi.org/10.1016/j.jmat.2019.12.012.

[17] S. Pratesi, M. De Lucia, M. Meucci, E. Sani, Structural and optical properties of copper-coated substrates for solar thermal absorbers, Superlattices and Microstructures. 98 (2016) 342–350. https://doi.org/10.1016/j.spmi.2016.08.031.

[18] R.L. Axelbaum, H. Brandt, The effect of substrate surface preparation on the optical properties of a black chrome solar absorber coating, Solar Energy. 39 (1987) 233–241. https://doi.org/10.1016/S0038-092X(87)80032-4.

[19] P. Kowalczewski, M. Liscidini, L.C. Andreani, Engineering Gaussian disorder at rough interfaces for light trapping in thin-film solar cells, Optics Letters. 37 (2012) 4868. https://doi.org/10.1364/OL.37.004868.

[20] A. Majumdar, B. Bhushan, Role of Fractal Geometry in Roughness Characterization and Contact Mechanics of Surfaces, Journal of Tribology. 112 (1990) 205–216. https://doi.org/10.1115/1.2920243.

[21] A. Majumdar, B. Bhushan, Fractal Model of Elastic-Plastic Contact Between Rough Surfaces, Journal of Tribology. 113 (1991) 1–11. https://doi.org/10.1115/1.2920588.

[22] F. Yang, R. Pitchumani, Interlaminar contact development during thermoplastic fusion bonding, Polymer Engineering & Science. 42 (2002) 424–438. https://doi.org/10.1002/pen.10960.

[23] Yu Bing-Xi, Zheng Na, Liang Zhong-Zhu, Li Ya-Nan, Liang Jing-Qiu, Fang Wei, Wang Wei-Biao, Design and preparation of black-nickel film on the radiometer chip, Acta Physica Sinica. 59 (2010) 4530. https://doi.org/10.7498/aps.59.4530.

[24] Su Fa-Gang, Liang Jing-Qiu, Liang Zhong-Zhu, Zhu Wan-Bin, Study on the surface morphology and absorptivity of light-absorbing materials, Acta Physica Sinica. 60 (2011) 057802. https://doi.org/10.7498/aps.60.057802.

[25] C. Niu, T. Zhu, Y. Lv, Influence of Surface Morphology on Absorptivity of Light-Absorbing Materials, International Journal of Photoenergy. 2019 (2019) 1–9. https://doi.org/10.1155/2019/1476217.

[26] M.C. Kang, J.S. Kim, K.H. Kim, Fractal dimension analysis of machined surface depending on coated tool wear, Surface and Coatings Technology. 193 (2005) 259–265. https://doi.org/10.1016/j.surfcoat.2004.07.020.

[27] S. Hatte, R. Pitchumani, Fractal Model for Drag Reduction on Multiscale Nonwetting Rough Surfaces, Langmuir. 36 (2020) 14386–14402. https://doi.org/10.1021/acs.langmuir.0c02790.

[28] R. Jain, R. Pitchumani, Fractal Model for Wettability of Rough Surfaces, Langmuir. 33 (2017) 7181–7190. https://doi.org/10.1021/acs.langmuir.7b01524.

[29] F.M. Borodich, A.B. Mosolov, Fractal roughness in contact problems, Journal of Applied Mathematics and Mechanics. 56 (1992) 681–690. https://doi.org/10.1016/0021-8928(92)90054-C.

[30] H. Wieder, A.W. Czanderna, Optical Properties of Copper Oxide Films, Journal of Applied Physics. 37 (1966) 184–187. https://doi.org/10.1063/1.1707803.

[31] N. Özer, F. Tepehan, Structure and optical properties of electrochromic copper oxide films prepared by reactive and conventional evaporation techniques, Solar Energy Materials and Solar Cells. 30 (1993) 13–26. https://doi.org/10.1016/0927-0248(93)90027-Z.

[32] N.R. Dhineshbabu, V. Rajendran, N. Nithyavathy, R. Vetumperumal, Study of structural and optical properties of cupric oxide nanoparticles, Applied Nanoscience. 6 (2016) 933–939. https://doi.org/10.1007/s13204-015-0499-2.

[33] S.S. Falahatgar, F.E. Ghodsi, F.Z. Tepehan, G.G. Tepehan, İ. Turhan, Electrochromic performance, wettability and optical study of copper manganese oxide thin films: Effect of annealing temperature, Applied Surface Science. 289 (2014) 289–299. https://doi.org/10.1016/j.apsusc.2013.10.153.

[34] W. V. Goodell, J.K. Coulter, P.B. Johnson, Optical constants of Inconel alloy films, Journal of the Optical Society of America. 63 (1973) 185. https://doi.org/10.1364/JOSA.63.000185.

[35] S.S. Aćimović, Setting excitation in 3D, Optical Proprties of Graphene. (2022). http://srdjancomsol.weebly.com/setting-excitation-in-3d.html (accessed June 24, 2022).

[36] COMSOL, Comsol, COMSOL Multiphysics User's Guide. (2020). http://www.comsol.com. (accessed March 13, 2021).

[37] A. Haghdoost, R. Pitchumani, M. Kargar, Fabricating Porous Metallic Coatings Via Electrodeposition and Compositions Thereof, US20210309870A1(Pending), 2021. https://patents.google.com/patent/US20210309870A1.

[38] R. Pitchumani, S.K. Purayil, Fractal Textured High Efficiency Solar Absorber Coatings, U.S. Provisional Patent No. 63/329,842., 2022.

[39] A. Haghdoost, R. Pitchumani, Fabricating Superhydrophobic Surfaces via a Two-Step Electrodeposition Technique, Langmuir. 30 (2014) 4183–4191. https://doi.org/10.1021/la403509d.

[40] Gwyddion, Gwyddion – Free SPM (AFM, SNOM/NSOM, STM, MFM, …) data analysis software, (2021). http://gwyddion.net/ (accessed January 21, 2022).

[41] A.D. Rakić, A.B. Djurišić, J.M. Elazar, M.L. Majewski, Optical properties of metallic films for vertical-cavity optoelectronic devices, Applied Optics. 37 (1998) 5271. https://doi.org/10.1364/AO.37.005271.

[42] N. Özer, F. Tepehan, Structure and optical properties of electrochromic copper oxide films prepared by reactive and conventional evaporation techniques, Solar Energy Materials and Solar Cells. 30 (1993) 13–26. https://doi.org/10.1016/0927-0248(93)90027-Z.

[43] C.K. Ho, A.R. Mahoney, A. Ambrosini, M. Bencomo, A. Hall, T.N. Lambert, Characterization of Pyromark 2500 Paint for High-Temperature Solar Receivers, Journal of Solar Energy Engineering. 136 (2014). https://doi.org/10.1115/1.4024031.

[44] J.F. Torres, K. Tsuda, Y. Murakami, Y. Guo, S. Hosseini, C.-A. Asselineau, M. Taheri, K.

Drewes, A. Tricoli, W. Lipiński, J. Coventry, Highly efficient and durable solar thermal energy harvesting via scalable hierarchical coatings inspired by stony corals, Energy & Environmental Science. 15 (2022) 1893–1906. https://doi.org/10.1039/D1EE03028K.